Plasmonic Electromagnetic Hot Spots Temporally Addressed by Photoinduced Molecular Displacement†

Mathieu L. Juan,‡,⊥ Jérome Plain,*,‡ Renaud Bachelot,‡ Alexandre Vial,‡ Pascal Royer,‡ Stephen K. Gray,§ Jason M. Montgomery,§ and Gary P. Wiederrecht¶

Laboratoire de Nanotechnologie et d'Instrumentation Optique, ICD CNRS FRE 2848, Université de Technologie de Troyes, BP 2060, Troyes, France, and Chemical Sciences and Engineering Division and Center for Nanoscale Materials, Argonne National Laboratory, Argonne, Illinois 60439

Received: December 27, 2008; Revised Manuscript Received: February 6, 2009

We report the observation of temporally varying electromagnetic hot spots in plasmonic nanostructures. Changes in the field amplitude, position, and spatial features are induced by embedding plasmonic silver nanorods in the photoresponsive azo-polymer. This polymer undergoes cis−trans isomerization and wormlike transport within resonant optical fields, producing a time-varying local dielectric environment that alters the locations where electromagnetic hot spots are produced. Finite-difference time-domain and Monte Carlo simulations that model the induced field and corresponding material response are presented to aid in the interpretation of the experimental results. Evidence for propagating plasmons induced at the ends of the rods is also presented.

Introduction

Localized surface plasmons (LSPs) have garnered a great amount of interest as drivers of unique photochemical and photophysical phenomena and have enabled ultrasensitive spectroscopies such as surface-enhanced Raman spectroscopy.[1,2] The general reason that LSPs are of such interest is that the field enhancement at the metal surface can produce local fields with an enhancement factor up to 10^3 and possibly higher. The great potential for these local fields is underscored by the fact that many light-induced chemical and physical processes, including Raman scattering, vary nonlinearly with the incident field amplitude. As a result, many structures have been designed to optimize and control the amplitude and spatial profile of the localized electromagnetic hot spots (EHs).[3−9] However, the magnitude of the field frequently depends on nanostructured variations with feature sizes smaller than what can be reasonably controlled with standard fabrication or synthesis techniques. Another possibility is that the surrounding dielectric medium is temporally varying, thereby altering the spatial features and amplitudes of the EHs and associated spectroscopic signals. Therefore, efforts to understand and control the EHs resulting from nanoscale defects would be valuable to the proposed applications of LSPs. In this article, we present an experiment that produces large and measurable variations of EHs in metal nanostructures, not only affecting the spatial profile of the EHs but also altering the position of the EHs on the nanostructure. Thus, the local environment is shown to change by a high enough degree to lead to the translation of the EHs on the metallic nanostructures.

The specific structures we consider are silver nanorods coated with the photoresponsive polymer DR1MA/MMA (poly[(methyl methacrylate)-*co*-(disperse red 1 methacrylate)]) with chemical structure shown in Figure 1. DR1MA/MMA is known to undergo mass transport under illumination, thereby producing a topographic reproduction of the spatial features of optical fields incident on the films.[10−13] This motion results from cycles of photoisomerization of the azobenzene groups covalently bound to the polymer backbone and is sensitive to both field gradient and polarization. We have recently extended these far-field illumination studies to include nanoscale plasmonic structures, in an effort to image the spatial features of EHs that are present on the nanostructures.[14,15] Of particular relevance to optical near

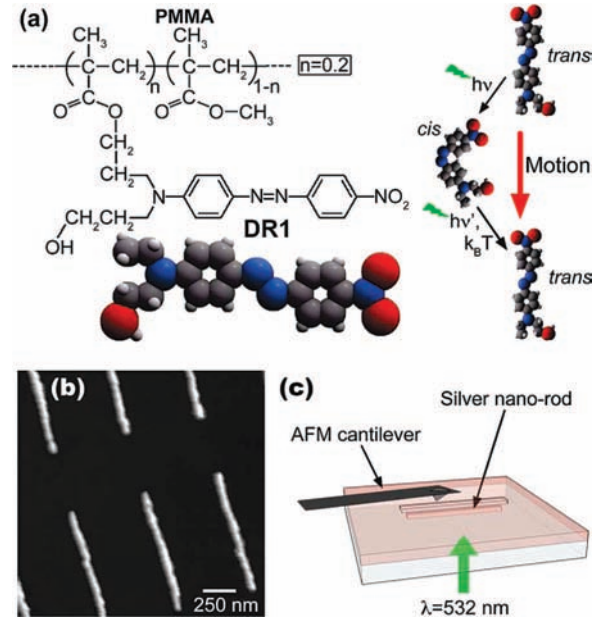

Figure 1. Principle of the experiment. (a) Chemical structure showing the azobenzene grafted to a chain of PMMA and the photoinduced motion via a trans−cis−trans isomerization cycle. (b) $2 \times 2\ \mu m^2$ atomic force microscopy image of silver nanorods produced by e-beam lithography. (c) The sample is covered by DR1MA/MMA, laser-illuminated, and characterized by atomic force microscopy.

† Part of the "George C. Schatz Festschrift".

* To whom correspondence should be addressed. E-mail: jerome.plain@utt.fr.

‡ Université de Technologie de Troyes.

§ Chemical Sciences and Engineering Division and Center for Nanoscale Materials, Argonne National Laboratory.

¶ Center for Nanoscale Materials, Argonne National Laboratory.

⊥ Current address: ICFO-Institut de Ciènces Fotòniques, 08860 Castelldefels, Barcelona, Spain.

10.1021/jp8114435 CCC: $40.75
Published on Web 03/18/2009

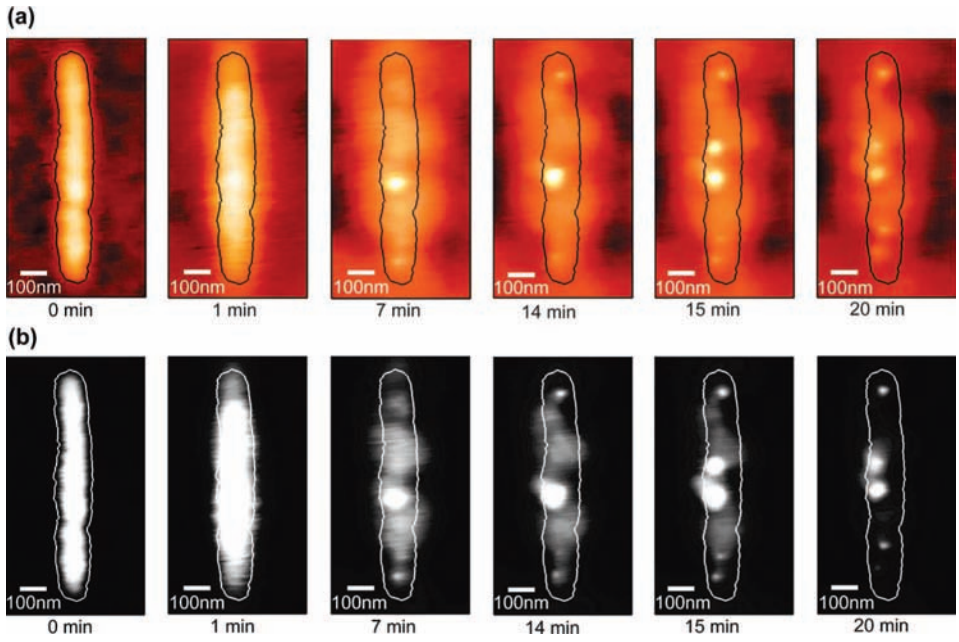

Figure 2. AFM images (0.57 × 1.21 μm^2) of the sample at different times: (a) raw data; (b) data for which a threshold was numerically applied.

fields, we showed that lateral optical fields lead to depletion where the field amplitude is maximum, whereas longitudinal fields lead to high topographical structures, as a result of the free space requirement of the molecules.[15] Thus, the strong anisotropies in the DR1MA/MMA transport characteristics enable the material to reveal the polarization components of the total optical near-field spatial profile.[15] In the experiments reported here, we have used this hybrid metal/organic material to visualize the EHs resulting from LSPs supported by local roughness on silver nanorods. The mass transport induced in the DR1MA/MMA produces a large and temporally varying dielectric medium around the nanostructure. The cycling relationship between the EHs and the changing film topography lead to EHs that disappear and reappear at new locations on a time scale of minutes. In this way, the EHs are successively transported along the nanorods. In this paper, we also quantify and model the dielectric constant modifications and the parameters that determine the individual EH location and spatial features.

Our approach is illustrated in Figure 1. An array of 1 μm long and 50 nm wide and high silver nanorods (SNR) were fabricated by electron beam lithography (Figure 1b). Compared to chemically synthesized structures, the fabricated nanorods are believed to be polycrystalline and to possess defects and roughness on their surfaces. These qualities can support EHs through LSP resonances in the roughened areas.[16,17] A 75 nm thick layer of DR1MA/MMA was deposited onto the sample. Atomic force microscopy (AFM) profiles show that the rods induced a topography 15 nm thick. The resulting organic/metallic system was illuminated for 1 min by a collimated laser beam (doubled frequency Nd:YAG laser, $\lambda = 532$ nm, $I = 100$ mW/cm^2) linearly polarized along the rod axis. After exposure, optically induced topography was characterized in situ by atomic force microscopy. The cycle (exposure + AFM imaging) was performed every minute, leading to 20 AFM images, each of them corresponding to an integrated exposure time T in the 0−20 min range. It should be pointed out that the laser was off during any AFM imaging.

Figure 2a is an example of a set of AFM images for $T = 0$ s, 1 min, 7 min, 14 min, 15 min, and 20 min and shows the time evolution of the sample topography. At $T = 0$ s the AFM shows a rod homogeneously capped by a thin layer of DR1MA/MMA. We focus our discussion here on a single nanorod, as all of the nanorods illustrate similar behavior. For clarity, the initial topography above the nanorod will be reproduced in each of the following images. At $T = 1$ min, the general topography was altered as a result of the effect of local electromagnetic field. This change occurs through a decrease of the contrast in the AFM image of the rod. As we will further show, the photosensitive polymer initially tends to migrate away from the rods as a consequence of the incident illumination field being linearly polarized. This molecular evacuation is illustrated by zones appearing darker, compared to $T = 0$ s, in the AFM image. At $T = 7$ min, a spot of high topograghy illustrating the sudden presence of a localized EH is observed above the surface of the rod. The lateral size is about 50 nm. At $T = 14$ min, two smaller spots appear at the extremities of the rod, in addition to the initial spot that appeared after 7 min of exposure. These three spots are found to be stable once visible and remain identical upon further exposure. In contrast, another major spot appears at $T = 15$ min near the initial spot, which begins to vanish at $T = 20$ min. Thus, we find that nanometric topographical spots appear and disappear at specific places at the top surface of the SNR as a function of time. For the case shown in Figure 2b, a numerical threshold of 8 nm was applied to the AFM images to emphasize the time evolution of the elevated spots. Figure 2b gives insight into three points. First, the general apparent surface nanorod topography decreases from $T = 0$ s to $T = 7$ min, showing that the thickness of the DR1MA/MMA layer tends to decrease above the rods. Second, some nanometer-sized spots appear as a function of time. For example, two nanospots (NS) appear from $T = 5$ min to $T = 7$ min. Third, some nanospots become smaller or even disappear as time evolves.

At this point, we can differentiate between two types of topographic spots regarding their size, position, and evolution during exposure: small spots at the extreme ends of the rod showing good temporal stability and large spots above the rod, many of which are highly dynamic once formed. With regard to the extremal features, even though the rod cannot support

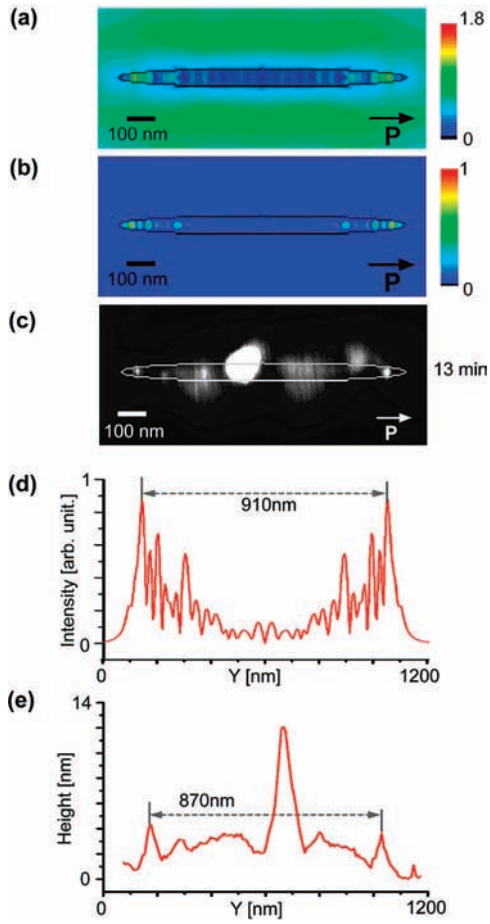

Figure 3. Impact of the longitudinal component of the field. Calculated (a) transverse and (b) longitudinal field of the nanorod using a FDTD method and (c) the experimental topography obtained after a 13 min exposure. (d) and (e) present the profiles taken above the nanorod along the length of the calculated longitudinal field and the experimental topography, respectively.

plasmon resonances for the incident wavelength and polarization, finite-difference time-domain (FDTD) calculations of the electric field (Figures 3a and 3b) reveal confined longitudinal fields at the extremities of the rod. The shape of the rod was approximated by an ellipse in the *XY* plane with a thickness of 50 nm with a discretization cell of $5 \times 5 \times 5$ nm^3. The scattering at the extremities produce several plasmon modes through the creation of additional wavevectors ($k_{scatter}$) that propagate over a small distance in the rod toward the opposite extremity. These modes, maximum in intensity at the launch sites (i.e., the extremities), interfere with the incident field, inducing the obtained dent shape in the calculation. However, the rapid decay of these modes prevent a resonance from forming over the length of the rod. It is important to note that the numeric structure used for the field calculation is slightly different from the actual experimental structure. Yet, these calculations provide a good approximation since the experimental structure presents similar extremities where the radii of curvature are likely to induce the higher wavevectors and act as plasmon launch sites. We now address the likeliness of the electric field components to induce topographic modifications. On the one hand, the transverse component ($|\mathbf{E}_X|^2 + |\mathbf{E}_Y|^2$) presents very little field gradient in the vicinity of the structure. The mass migration induced by this component is not expected to induce noticeable topographic migration. Nanoscale defects that do not show a plasmon resonance overlapping the absorption spectrum of DR1MA/MMA will not therefore produce measurable topographic

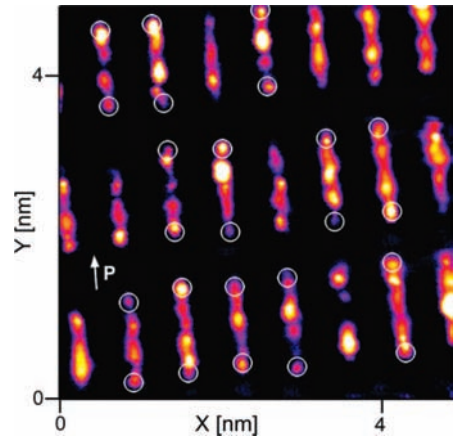

Figure 4. Large area AFM characterization of photoinduced topography after 20 min exposure. The photochemical imaging of longitudinal components of the electric field on several rods is outlined by the white circles.

changes to the polymer film. On the other hand, both the transverse and longitudinal ($|\mathbf{E}_Z|^2$) components of the electric field present high-intensity regions above the rod, when near the extremities. Under these conditions, previous work underscores the affinity of the DR1MA/MMA to react preferably to longitudinal components of the field even for small contribution.[18] This effect is related to free space considerations regarding the translation quantum yield of the pseudostilbene molecules. Accounting for this effect, one can predict the topographic modifications to be primarily linked to the longitudinal component of the field. Since longitudinal components induce matter accumulation rather than topographic depressions,[15,18] the photoinduced topography should present elevated spots at the high-intensity region of the longitudinal component. Figure 3c presents the thresholded topography obtained after a 13 min exposure. The shape of the nanorod used for the calculation (seen in black in Figures 3a and 3b and in white in Figure 3c) emphasizes the relative position of the extremal topographic spots. The calculated spacing between the extremal hot spots is in very good agreement with the observed spacing: 910 and 870 nm, respectively. For the examined rod, the extremal spots are related to the longitudinal component of the field induced at the extremities of the rod.

Since the experiment was performed on an array of nanorods, Figure 4 shows a large field AFM characterization of the sample after a 20 min exposure to highlight the large number of rods exhibiting extremal spots. The presence of these spots on several rods confirms that the DR1MA/MMA experiments can reveal the particular electric field induced by the rods. In this context, photochemical imaging appears to be a relevant method to characterize the longitudinal component of the field even for low intensity. Indeed, the calculated normalized intensity of the localized longitudinal fields at the extremities of the rod is 1: no strong enhancement is observed. Yet, both the presence of major spots randomly placed above the rods and the nanofabrication process can, in some locations, prevent the formation of extremal spots.

We now consider an interpretation of the observations seen in Figures 2 and 3. The large area AFM characterization (Figure 4) underscores the random aspect of the NS. This excludes the extremal protrusions, since the longitudinal fields produced in these regions are not as strongly temporally varying and are due to the longer scale rod structure as summarized in Figure 3 and supporting text. We argue that the observed nanometer-

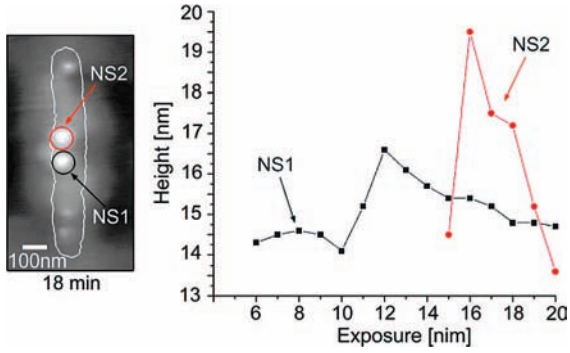

Figure 5. Time evolution of two specific electromagnetic hot spots. Height of nanospots NS1 and NS2 as observed by atomic force microscopy (the label is defined on the AFM image on the left side).

sized topographical structures result from the excitation of resonant plasmonic electromagnetic hot spots supported by nanometer scale roughness localized at the top surface of the nanorods (Figure 1b). DR1MA/MMA is known to enable controlled, optically assisted molecular migration. In particular, it has been shown that while lateral fields lead to an escape of matter from bright zones, longitudinal fields tend to locally lift the matter as a result of the free space requirement from the molecules. These electromagnetic hot spots, supported by local roughness on silver nanorods, present strong longitudinal components likely to induce the observed nanospots. This ability of the electromagnetic hot spots to turn on and then turn off is clearly illustrated in Figure 5, for which we temporally followed two specific nanospots labeled as NS1 and NS2. NS1 is almost a steady-state, temporally invariant feature with a height between 14 and 16.5 nm. It is important to note that the AFM characterization does not provide true zero altitude. The topographic singularity's height is given with reference to the minimal height of the polymer surrounding the structure. In comparison with the height evolution of NS1, NS2 shows a rapid evolution during the exposure. While no singularity is visible before 15 min of exposure, NS2 quickly appears during the 16th minute. Moreover, the height of NS2 reaches a higher value than that of NS1, suggesting a more intense electromagnetic hot spot.

Considering the fast appearance/disappearance dynamics exhibited by NS2, one can consider the spectral shift of the defect resonances induced by the polymer migration during exposure. Indeed, under the effect of the linearly polarized illumination field, the polymer tends to migrate out from the rods. These topographic modifications are likely to induce important changes in the effective index due to the high effective index of the polymer ($n_{\mathrm{DR1MA/MMA}} = 1.7$). At this point, it is possible to estimate this mass migration induced spectral shift,[19]

$$\Delta\lambda_{\max} = m\Delta n\left(1 - \exp\left(-\frac{2d}{l_{\mathrm{d}}}\right)\right) \qquad (1)$$

where $\Delta\lambda_{\max}$ is the spectral shift, m the refractive index sensitivity of the structure, Δn the refractive index difference between the two media ($\Delta n = n_{\mathrm{DR1MA/MMA}} - n_{\mathrm{air}} = 0.7$), d the thickness of polymer, and l_{d} the characteristic decay length of the electromagnetic field.

Yet some of these values are difficult to estimate. First, regarding the value of the refractive index sensitivity, one can use the existing values provided in the literature.[20,21] While silver structures show slightly lower sensitivity, the increasing complexity or the aspect ratio of the structures provide an efficient way to obtain high sensitivity (e.g., m = 700 nm RIU^{-1} has been reported for gold nanobranches). In our experiment, to account for the complexity and variety of defects likely to induce EHs, we assumed the sensitivity to be important and used a high value of $m = 500$ nm RIU^{-1}. Concerning the characteristic decay length of the electromagnetic field, it is interesting to evaluate whether the lateral size of the induced topographic spot gives information on the spatial conformation of the EHs. To this end, we used a Monte Carlo based model[22] to evaluate the relation between the topographic spot size and the EHs characteristic decay length. Figure 6 presents the simulated topography for different EH size. The electric field used in this simulation was a longitudinal field which exhibited three different EHs (Figure 6a). We first emphasize the global shape of the calculated topographic spots (Figures 6b and 6c). They are similar to the experimental topographic spots, confirming the idea that these spots are related to the longitudinal components of the field. In addition, the lateral size of the calculated topographic spots is directly related to the extension of the electric field. Indeed, the matter accumulation induced by the longitudinal component mainly occurs in high-intensity regions; thus, the topographic spot will have dimension commensurate with the electric field. This suggests the possibility to assess the characteristic decay length of the EHs from the experimentally obtained topographies.

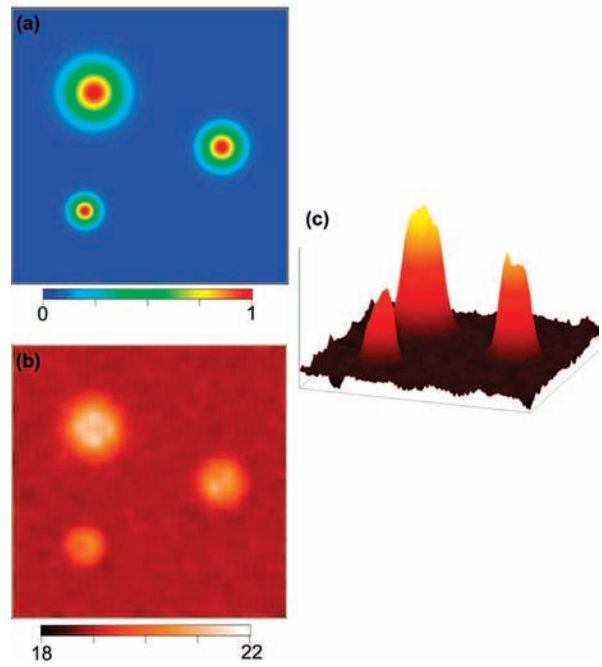

Figure 6. Simulated topographic spots: (a) electric hot spots of different size; (b and c) the simulated topography shows spots whose lateral sizes are related to the spatial extension of the field.

The Monte Carlo based migration model provides useful insight into the relation between the topographic spot size and the electric field decay length. It is now relevant to examine the experimental topographies in light of these simulations. The various topographic spots exhibit different lateral sizes (Figure 7a). The size of an extremal topographic spot is compared to the spatial extension of the longitudinal component of the field (Figure 7c and 7d). In good agreement with the numerical results, the lateral size of the spot is directly related to the confinement of the field. The mass accumulation, under the effect of a longitudinal field, thus provides an interesting method to determine the degree of confinement of the electric field. From

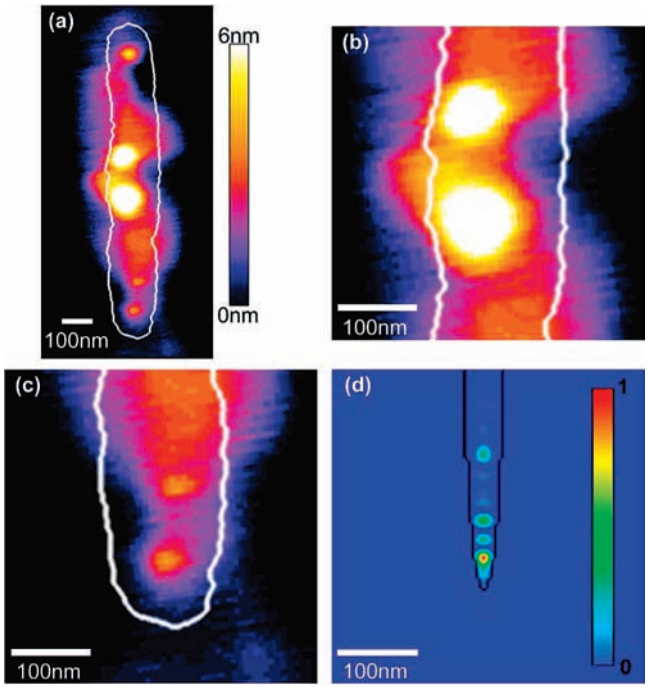

Figure 7. Experimental lateral size of the topographic spots: (a) Photoinduced topography after 13 min exposure; the image has been numerically processed to underline the spot lateral size. (b) Magnification of the EHS induced topographic spot (previously labeled NS1 and NS2).

the lateral size of the topographic spots NS1 and NS2 (enlarged Figure 7b) one can estimate the value of l_d. To account for the variety of defect-induced EHs, we use two different values: $l_d = 10$ nm and $l_d = 15$ nm. Regarding the initial DR1MA/MMA thickness (70 nm) and the initial topography above the structure, we can deduce the polymer thickness above the structure. We have previously emphasized that, during the exposure, mass migration due to the incident field tends to reduce the topography. This large scale mass migration (Gaussian beam migration)[23] reduces the polymer thickness above the structure by 15 nm. From these values, the spectral shifts at resonance for EH active defects are

$$l_d = 10 \text{ nm}: \ \Delta\lambda_{max} \simeq 16 \text{ nm}$$

$$l_d = 15 \text{ nm}: \ \Delta\lambda_{max} \simeq 40 \text{ nm}$$

It appears from these simple considerations that the mass migration can induce strong spectral shifts likely to induce appearance/disappearance of EHs. However, the variety and complexity of the surface defects present in our samples does make it difficult to precisely reproduce specific experimental EH variations with our modeling approach. Small local variations in nanodefect density or polymer thickness could produce larger spectral shift changes near one defect as compared to another, thus leading the different temporal profiles underscored by the NS1 and NS2 example.

In conclusion, photochemical imaging performed using the DR1MA/MMA leads to two important insights. First, this experimental approach provides a tool to map longitudinal fields induced by metallic nanostructures, even for small amplitudes due to the sensitivity of the material response to movement out of the plane of the film. It would be of great interest to carry out such experiments on a variety of nanostructures, in particular, nanoantennas, to provide information on the confinement of the longitudinal field. Second, the time scale of mass migration observed in our experiments provides a new approach to force EH dynamics and appearance/disappearance to be on the order of the minute time scale. The position and movement of appearing EHs is thus revealed through the topographic spots. By optimizing the material response, the nanostructures, and the illumination field parameters, this hybrid system may yield a new means to control the appearance and amplitude of electromagnetic hot spots in plasmonic systems.

Acknowledgment. One of the authors' Ph.D. research (M.J.) is supported by the European Social Fund and the Conseil Général de l'Aube (distric grant). This work was financially supported by the ANR (2007 Photohybrid) and the Région Champagne-Ardennes (Project E2007-08052). Use of the Center for Nanoscale Materials and work at Argonne National Laboratory were supported by the U.S. Department of Energy, Office of Science, Office of Basic Energy Science, under Contract No. DE-AC02-06CH11357.

References and Notes

(1) Otto, A.; Mrozek, I.; Grabhorn, H.; Akemann, W. *J. Phys.: Condens. Matter* **1992**, *4*, 1143.
(2) Schatz, G.; Young, M.; Van Duyne, R. *Top. Appl. Phys.* **2006**, *103*, 19–46.
(3) Shimizu, K.; Pala, R.; Fabbri, J.; Brongersma, M.; Melosh, N. *Nano Lett.* **2006**, *6*, 2767.
(4) Willets, K.; Van Duyne, R. *Annu. Rev. Phys. Chem.* **2007**, *58*, 267.
(5) Hofmann, C.; Vesseur, E.; Sweatlock, L.; Lezec, H.; Garcia de Abajo, F.; Polman, A.; Atwater, H. *Nano Lett.* **2007**, *7*, 3612.
(6) Lai, S.; Grady, K.; Kundu, J.; Levin, C.; Lassiter, J.; Halas, N. *Chem. Soc. Rev.* **2008**, *37*, 898.
(7) Genuche, P.; Cherukulappurath, S.; Taminiau, T.; Van Hulst, N.; Quidant, R. *Phys. Rev. Lett.* **2008**, *101*, 116805.
(8) Hoppener, C.; Novotny, L. *Nano Lett.* **2008**, *8*, 642.
(9) Le Ru, E.; Grand, J.; Felidj, N.; Aubard, J.; Levi, G.; Hohenau, A.; Krenn, J.; Blackie, E.; Etchegoin, P. *J. Phys. Chem. C* **2008**, *112*, 8117.
(10) Rochon, P.; Batalla, E.; Natansohn, A. *Appl. Phys. Lett.* **1995**, *66*, 136–138.
(11) Kim, D. Y.; Tripathy, S. K.; Li, L.; Kumar, J. *Appl. Phys. Lett.* **1995**, *66*, 1166–1168.
(12) Natansohn, A.; Rochon, P. *Chem. Rev.* **2002**, *102*, 4139–4175.
(13) Cojocariu, C.; Rochon, P. *Pure Appl. Chem.* **2004**, *76*, 1479–1497.
(14) Hubert, C.; Rumyantseva, A.; Lerondel, G.; Grand, J.; Kotscheev, S.; Billot, L.; Vial, A.; Bachelot, R.; Royer, P.; Chang, S.; Gray, S. K.; Wiederrecht, G.; Schatz, G. S. *Nano Lett.* **2005**, *5*, 615–619.
(15) Hubert, C.; Bachelot, R.; Plain, J.; Kotscheev, S.; Lerondel, G.; Juan, M.; Royer, P.; Zou, S.; Schatz, G. S.; Wiederrecht, G.; Gray, S. K. *J. Phys. Chem. C* **2008**, *112*, 4111–4116.
(16) Garcia Vidal, F.; Pendry, J. *Phys. Rev. Lett.* **1996**, *77*, 1163.
(17) Zayats, A.; Smolyaninov, I.; Maraududin, A. *Phys. Rep.* **2005**, *408*, 131.
(18) Gilbert, Y.; Bachelot, R.; Royer, P.; Bouhelier, A.; Wiederrecht, G.; Novotny, L. *Opt. Lett.* **2006**, *31*, 613–615.
(19) Riboh, J. C.; Haes, A. J.; McFarland, A.; Yonzon, C.; Van Duyne, R. *J. Phys. Chem. B* **2003**, *107*, 1772.
(20) Haes, A. J.; Van Duyne, R. *J. Am. Chem. Soc.* **2002**, *124*, 10596.
(21) Chen, H.; Kou, X.; Yang, Z.; Ni, W.; Wang, J. *Langmuir* **2008**, *24*, 5233.
(22) Juan, M.; Plain, J.; Bachelot, R.; Royer, P.; Gray, S.; Wiederrecht, G. *Appl. Phys. Lett.* **2008**, *93*, 153304.
(23) Viswanathan, N. L.; Kim, D. Y.; Bian, S.; Williams, J.; Liu, W.; Li, L.; Samuelson, L.; Kumar, J.; Tripathy, S. K. *J. Mater. Chem.* **1999**, *9*, 1941–1955.

JP8114435